metals

MDPI

Article

Compression and Tensile Testing of L-PBF Ti-6Al-4V Lattice Structures with Biomimetic Porosities and Strut Geometries for Orthopedic Implants

Dimitri P. Papazoglou [1,*], Amy T. Neidhard-Doll [1], Margaret F. Pinnell [2], Dathan S. Erdahl [3] and Timothy H. Osborn [4]

[1] Department of Electrical and Computer Engineering, University of Dayton, 300 College Park, Dayton, OH 45469, USA; aneidharddoll1@udayton.edu
[2] Department of Mechanical and Aerospace Engineering, University of Dayton, 300 College Park, Dayton, OH 45469, USA
[3] NDE Engineering Group, University of Dayton Research Institute, 300 College Park, Dayton, OH 45469, USA
[4] Additive Manufacturing Technology Development Group, University of Dayton Research Institute, 300 College Park, Dayton, OH 45469, USA
* Correspondence: papazoglou6@gmail.com or papazoglou.2@osu.edu

Abstract: In an effort to contribute to the ongoing development of ASTM standards for additively manufactured metal lattice specimens, particularly within the field of medicine, the compressive and tensile mechanical properties of biomimetic lattice structures produced by laser powder bed fusion (L-PBF) using Ti-6Al-4V feedstock powder were investigated in this research. The geometries and porosities of the lattice structures were designed to facilitate internal bone growth and prevent stress shielding. A thin strut thickness of 200 μm is utilized for these lattices to mimic human cancellous bone. In addition to a thin strut size, two different strut geometries were utilized (cubic and body-centered cubic), along with four different pore sizes (400, 500, 600, and 900 μm, representing 40–90% porosity in a 10 mm cube). A 10 mm^3 cube was used for compression testing and an experimental pin-loaded design was implemented for tensile testing. The failure mode for each specimen was examined using scanning electron microscopy (SEM). Lattice structures were compared to the mechanical properties of human cancellous bone. It was found that the elastic modulus of human cancellous bone (10–900 MPa) could be matched for both the tensile (92.7–129.6 MPa) and compressive (185.2–996.1 MPa) elastic modulus of cubic and body-centered cubic lattices. Body-centered cubic lattices exhibited higher compressive properties over cubic, whereas cubic lattices exhibited superior tensile properties. The experimental tensile specimen showed reacquiring failures close to the grips, indicating that a different tensile design may be required for consistent data acquisition in the future.

Keywords: lattice structure; orthopedic implants; selective laser melting; additive manufacturing; Ti-6Al-4V

Citation: Papazoglou, D.P.; Neidhard-Doll, A.T.; Pinnell, M.F.; Erdahl, D.S.; Osborn, T.H. Compression and Tensile Testing of L-PBF Ti-6Al-4V Lattice Structures with Biomimetic Porosities and Strut Geometries for Orthopedic Implants. *Metals* **2024**, *14*, 232. https://doi.org/10.3390/met14020232

Academic Editor: Jürgen Eckert

Received: 17 December 2023
Revised: 9 February 2024
Accepted: 9 February 2024
Published: 14 February 2024

1. Introduction

The lattice structure, also known as an open-cellular structure, is a complex three-dimensional arrangement of repeating unit cells with distinctive properties such as a high stiffness-to-weight ratio, negative Poisson's ratio, low coefficient of thermal expansion, viscoelastic response, and increased heat dissipation [1]. While traditional manufacturing methods such as casting and forging are advantageous in the production of large quantities of parts with a restricted number of shapes and sizes, they are limited in terms of the ability to produce custom patient-specific parts with complex 3D geometries such as lattices. Powder bed fusion using a laser beam (PBF-LB) and similar additive manufacturing (AM) technologies such as powder bed fusion using an electron beam (PBF-EB) offer a potential solution for high-risk load-bearing applications in the automotive,

aerospace, and medical industries. In recent years, biomimetic metallic lattice structures have been explored in the design of 3D-printed orthopedic implants for in vivo use using biocompatible titanium alloy feedstock powder (e.g., Ti-6Al-4V) [2–13]. However, the majority of these studies focus on surface morphology rather than mechanical testing since there are currently no standards for compression or tensile testing published by the American Society for Testing and Materials (ASTM) for metal additive manufacturing or AM-produced metallic lattice structures, especially in biocompatible materials such as Ti-6Al-4V in the field of medicine.

A reoccurring problem associated with traditional orthopedic implants is stress shielding, where the high elastic modulus of the implant 'shields' the residual bone from mechanical loading. In response to this reduction in stress, the residual bone reduces normal remodeling efforts (Wolff's law) and a decrease in bone mass is observed over time. This can result in implant loosening and eventual failure [14]. Biomimetic lattice structures inspired by the porous (75–95%) network of interconnected rods and plates found in human cancellous bone may offer a potential solution [15]. The elastic modulus of a 3D-printed lattice structure orthopedic implant can be customized for individual patient needs by tuning the porosity and/or the unit cell geometry, thereby reducing stress-shielding and improving the overall outcome for the patient.

Another biological benefit of employing lattice structures for orthopedic implants is the formation of internal and external bone growth, known as osteogenesis. The traditional non-porous implant will only facilitate external bone growth. For biomimetic lattice structures, the extracellular matrix can grow into the body of the implant, which results in a greater level of osseointegration when compared to non-porous implants. The benefit of this internal bone growth is the improved mechanical interlocking of bone to the implant, which improves the secondary stability of the implant [16,17]. The pore size range for promoting osteogenesis is 400–1000 μm, in which numerous additively manufactured lattices have been demonstrated with in vivo and in vitro studies [18–29].

Compression testing data for lattice structures with unit cell geometries such as gyroid [1,2,30,31], cubic [30,32,33], octahedral [34], body-centered cubic (BCC) [35,36], and diamond [9] are well documented in the literature; however, tensile data are limited [30]. This may be due to challenges associated with the design of a tensile specimen for lattice structures [37]. Since the bones and joints of the human musculoskeletal system experience both compressive and tensile loading [38], assessing the tensile properties of orthopedic implant materials is vital for the development of these devices.

In this research, the compressive and tensile properties of biomimetic Ti-6Al-4V selective laser melted lattices of varying strut geometry and porosity were evaluated and compared to the mechanical properties of cancellous bone. To mimic cancellous bone, lattice structures were designed with a 200 μm strut thickness. An experimental tensile specimen design was created to evaluate tensile properties, along with a 10 mm^3 specimen for compressive properties. Two different strut geometries (cubic and body-centered cubic) and four different pore sizes (400, 500, 600, and 900 μm, representing 40–90% porosity in a 10 mm cube) were utilized. The porosities chosen for these lattices have been shown to promote internal bone growth for orthopedic implants [20–29]. In addition, structural characterization was performed using scanning electron microscopy (SEM).

2. Materials and Methods

2.1. Design of Lattice Structures

Eight biomimetic lattice structures were designed for this work with cubic and body-centered cubic (BCC) unit cell geometries (Figure 1). Biomimetic pore sizes of 400, 500, 600, and 900 μm were incorporated into each unit cell geometry. Each lattice featured a 200 μm strut thickness, except for compression specimen BCC 900 μm, which had a strut thickness of 400 μm. Preliminary testing indicated failures during the selective laser melting production of BCC 900 μm with 200 μm struts [39]. The computer-aided design (CAD) software used to produce the lattices was nTopology 3.0. Figure 2 illustrates the

compression specimens for each strut geometry and porosity, as produced in nTopology and as manufactured by selective laser melting, respectively. Lattices were designed to satisfy the Maxwell criteria (M) for bending-dominated structures (Cubic: M-6 and BCC: M-13) [40]. Most cellular structures (i.e., lattice structures) are classified as bending-dominated, due to the number of nodes and struts.

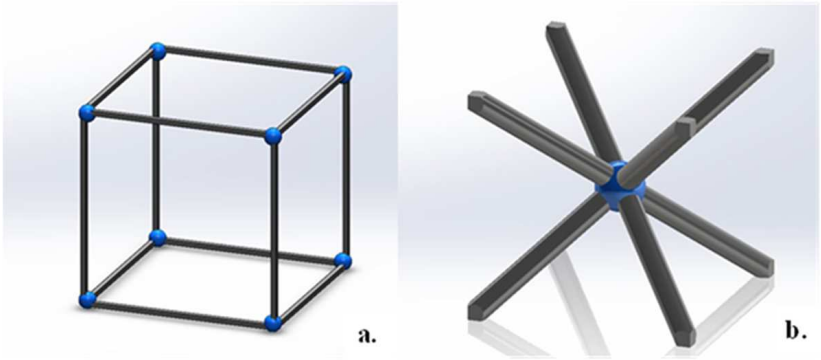

Figure 1. Unit cell geometry of cubic (**a**) and body-centered cubic (**b**). Reprinted from ref. [41].

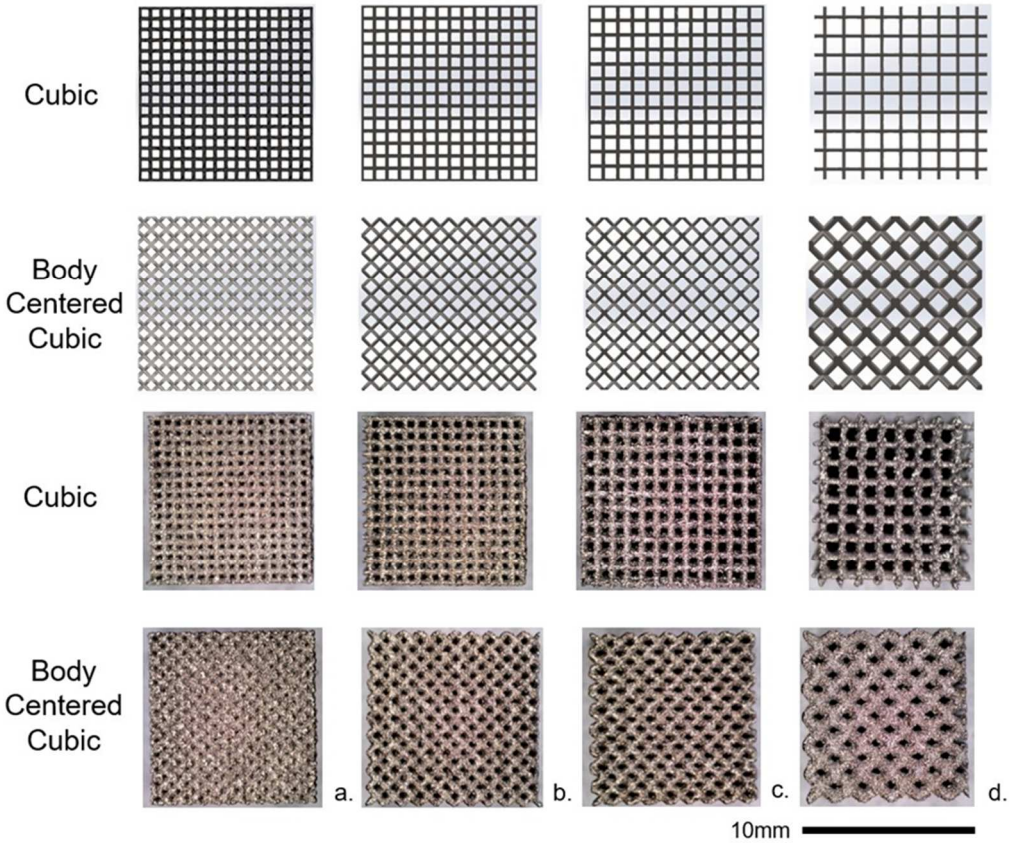

Figure 2. Images from CAD models (**top two rows**) and selective laser melting manufactured Ti-6Al-4V (**bottom two rows**) cubic and body-centered cubic lattices. Pore sizes: (**a**) 400 µm, (**b**) 500 µm, (**c**) 600 µm, and (**d**) 900 µm. Reprinted from ref. [41].

2.2. Materials and AM Processing Parameters

The powder utilized for selective laser melting was AP&C Ti-6Al-4V Grade 5, which was reused for nine builds prior to use for this work. The powder was sieved at 63 µm and 75 µm to maintain a consistent particle size distribution and remove any anomalous particles such as fused particles or oxidized particles. According to the ASTM Standard Guide for Powder Reuse Schema in Powder Bed Fusion Processes for Medical Applications

for Additive Manufacturing Feedstock Materials (ASTM F3456), the powder used in this study complies with the continuous reuse schema [42].

All lattice designs were manufactured using an open-architecture selective laser melting machine (DART; University of Dayton Research Institute, Dayton, OH, USA) with an IPG Photonics Continuous Wave 500 W laser. During the build, the laser power was set to 150 W, with a mark speed of 950 mm/s, and a bidirectional strip hatch with 6 mm titles and 0.08 mm spacing. The laser thickness was 40 µm. Oxygen content during the build was <0.1%. After each build was completed, the parts were heat-treated on the build plate at 800 °C (±10 °C) for 120 min (±30 min) in a vacuum (1.3×10^{-3}–1.3×10^{-5} mbar), followed by cooling under vacuum. The lattices were removed from the build plate by electron discharge machining.

Compression samples were 10 mm^3 cubes, while the tensile specimens (Figure 3) incorporated an experimental pin-loaded design that was previously tested with Nylon 12 by Porter et al. [43]. Tensile specimen dimensions were 20 × 20 × 60 mm, featuring a gauge section of 20 mm^3. All tensile specimens were printed in a vertical orientation (along the Z-axis).

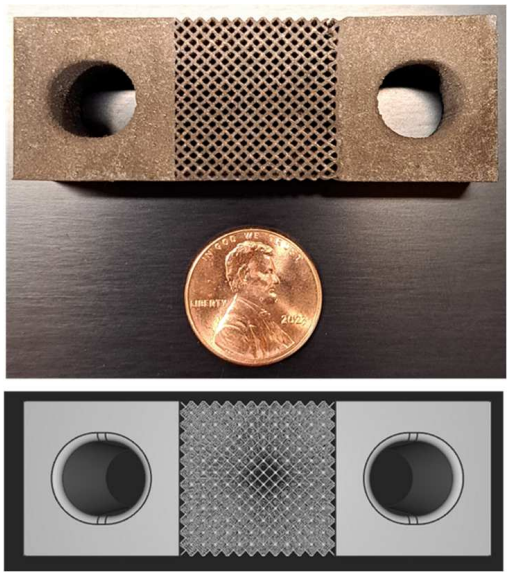

Figure 3. Selective laser melting manufactured Ti-6Al-4V tensile specimen BCC 900 µm (**top**) and corresponding CAD model (**bottom**). Reprinted from ref. [41].

2.3. SEM Analysis

To investigate the accuracy of 3D-printed parts when compared to corresponding CAD models, scanning electron microscopy (SEM) analysis using a Hitachi TM3000 SEM (Tokyo, Japan) (15 kV) was performed on each of the lattices to measure the dimensions of pores and struts, as well as to observe the surface finish. Random images were selected and evaluated with ImageJ (version 1.54G), measurements were performed six times per sample, and the average of these measurements was used in the analysis. Relative density was measured and calculated for each lattice structure and can be defined as the ratio of lattice density (displacement method) to the reference density of Ti-6Al-4V (4.43 g/cm^3) [44].

2.4. Compression Testing

The compression test setup is shown in Figure 4a. Compression testing was performed at room temperature (20–22 °C) on an Instron 4486 (Norwood, MA, USA) equipped with a 30 kN load cell, using Instron Bluehill Universal V4.28 software for all specimens with the exception of BCC 400 µm. Compression testing for BCC 400 µm was performed with an MTS Alliance RF/300 (Eden Prairie, MN, USA) using a 300 kN load cell, as BCC 400 µm had exceeded the 30 kN load cell of the Instron 4486. Testing and measurements were

performed using the ASTM E9 standard as a guide [45]. The compression test utilized fixed compression plates as the test fixture. The test rate was set to 0.05 mm/min. The end of the test setting was a load greater than 40%. All 10 mm^3 lattice compression samples were compressed following the print direction (Z-axis). Stress–strain curves were generated for all samples and the results for modulus of elasticity (E), yield strength (σ_y), and compressive strength (σ_{max}) were reported. E was estimated with the rise over run (slope) of the stress–strain curve. σ_y was calculated using the 0.2% offset method. σ_{max} was reported as the highest stress value over the cross-sectional area of the specimen. The sample size for compression testing of each lattice porosity was three.

Figure 4. Compression testing setup (**a**) and tensile testing setup (**b**). Reprinted from ref. [41].

2.5. Tensile Testing

The tensile test setup is shown in Figure 4b. Tensile testing was performed with an Instron 4486 using 30 kN load cells and Instron Bluehill Universal V4.28 software for all specimens. Testing and measurements were performed using the ASTM E8/E8M standards as a guide [46]. An experimental test specimen design was implemented in addition to a custom machined fixture (4130 Steel) for this work as no standard tensile specimen for lattice structures currently exists [47], as shown in Figure 4b. The room temperature was around 20–22 °C. The test rate was set to 0.45 mm/s. The end-of-test setting was a peak load greater than 60%. Tensile testing was performed along the build direction (Z-axis) of the specimen. Modulus of elasticity (E), yield strength (σ_y), and tensile strength (σ_{max}) were recorded. Tensile strength was the maximum tensile force during tension, calculated with the original cross-sectional area of the gauge. Due to difficulties in manufacturing the tensile specimens, the sample size varied and is reported as two to three samples.

3. Results and Discussion

3.1. SEM Analysis

The selective laser melting manufactured 10 mm^3 lattices were analyzed using SEM to determine the deviations in pore size and strut diameter. SEM images can be seen in Figure 5, along with measured pore and strut size deviations in Table 1.

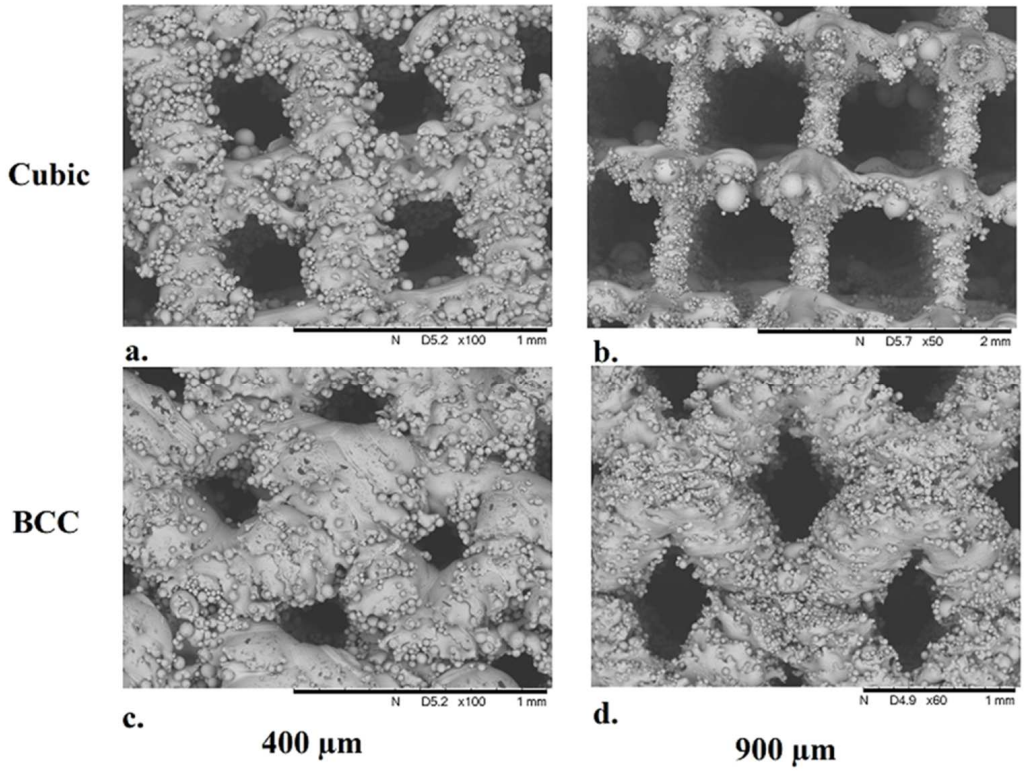

Figure 5. SEM images of 10 mm^3 Ti-6Al-4V lattice specimens with BCC (**top row**) and cubic (**bottom row**) unit cell geometries. Pore sizes: 400 µm (**a**,**c**) and 900 µm (**b**,**d**). Reprinted from ref. [41].

Table 1. Measurements and deviations of pore sizes and strut diameters were obtained from SEM images. Reprinted from ref. [41].

Lattice Type	Average Pore Size (µm)	Pore Size Deviation (%)	Average Strut Diameter (µm)	Strut Diameter Deviation (%)
Cubic P400	374.6 (±32.1)	−6.5	310.1 (±34.4)	43.1
Cubic P500	439.2 (±63.0)	−12.9	333.8 (±43.7)	49.9
Cubic P600	559.1 (±50.9)	−7.1	268.2 (±43.8)	29
Cubic P900	849.5 (±37.9)	−5.7	312.6 (±67.6)	43.7
BCC P400	219.2 (±49.1)	−58.3	428.5 (±37.0)	72.6
BCC P500	411.5 (±25.3)	−19.5	344.8 (±41.3)	52.9
BCC P600	533.6 (±37.1)	−11.8	375.5 (±30.1)	60.8
BCC P900	675.2 (±109.9)	−28.5	629.1 (±35.0)	44.5

Discrepancies between CAD models and as-produced parts are often found during the selective laser melting process due to unmelted particles from powder feedstock adhering to the surface [48]. As illustrated in Table 1, it was found that BCC lattices have larger deviations in pore size and strut diameter than the equivalent cubic lattices. This phenomenon is likely due to BCC lattices featuring 45° struts. These 45° struts have a lower thermal conductivity than 90° struts due to the down skin surface of the struts, resulting in a larger melt pool size from reduced heat dissipation, leading to an increased strut diameter. These larger-than-specified struts led to a decreased pore size [49]. In response to an increased strut diameter, the porosity of selective laser melting produced parts is substantially higher than designed lattices, as seen in Table 2.

Table 2. The weight, relative density, and porosity for CAD and selective laser melting manufactured cubic and BCC lattices. Averaged across three samples. Reprinted from ref. [41].

Lattice Type	CAD Weight (g)	Produced Weight (g)	CAD Relative Density (%)	Produced Relative Density (%)	CAD Porosity (%)	Produced Porosity (%)
Cubic P400	0.9	2.3	21	52	79.4	49.2
Cubic P500	0.7	1.6	17	40	83.8	63.3
Cubic P600	0.5	1.2	12	31	87.9	27.9
Cubic P900	0.2	0.6	7	12	93.1	92.1
BCC 400	1.0	2.8	25	65	75.8	14.9
BCC 500	0.8	1.7	19	44	81.9	61.6
BCC 600	0.6	1.4	15	37	85.3	64.7
BCC 900	1.0	1.7	25	44	75.2	77.8

3.2. Relative Density

Samples were weighed using a precision scale and compared to the CAD-designed theoretical weight, which was calculated using a function built into nTopology that references the density of Ti-6Al-4V (Table 2).

It was found that all lattices, with the exception of BCC 900, doubled in selective laser melting produced weight when compared to theoretical CAD values. The relative density can be seen in Figure 6 and Table 2. When comparing unit cell geometries, all four BCC lattices demonstrated a higher relative density when compared to their cubic counterparts of the same porosity. In Figure 6, the relative density for BCC 900 appears to be an anomaly when compared to the other specimens. This can be attributed to the fact that the strut thickness was double (400 μm) for the BCC 900 lattice specimens.

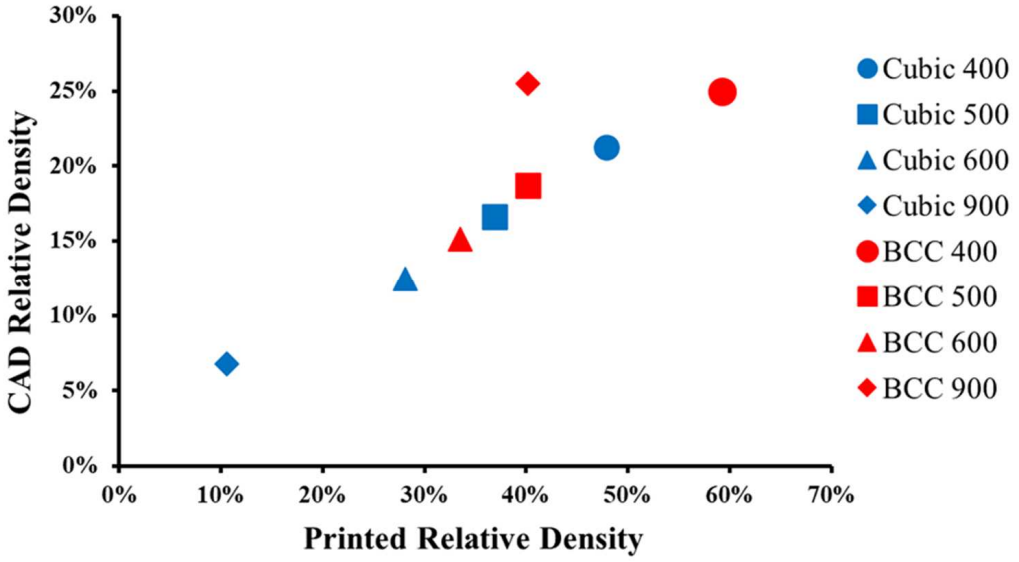

Figure 6. Comparison of CAD-designed relative density to printed relative density. Reprinted from ref. [41].

The differences between the relative density for CAD and as-produced lattices are considerable and may be attributed to the surface roughness (despite HIP) and the process parameters chosen for this study, such as the layer thickness (40 microns) or laser power [50]. However, while surface roughness is often an undesirable byproduct of the laser powder bed fusion process, it is advantageous in the design of orthopedic implants, providing additional surface area for the osseointegration of bone cells [51].

3.3. Compressive Response

The failure mode for cubic lattices (Figures 7 and 8) under compressive loading was found to be the collapse of an entire row (Cubic 500) or a combination of adjacent rows (Cubic 400). Choy et al. [33] observed a similar phenomenon of layer-by-layer failure in cubic selective laser-melted Ti-6Al-4V lattices of a larger pore size and strut thickness. In the case of Cubic 900 µm, the lattice structure became brittle and separated into multiple pieces at the failure point. This is due to a lower number of struts and nodes when compared to specimens with smaller pore sizes.

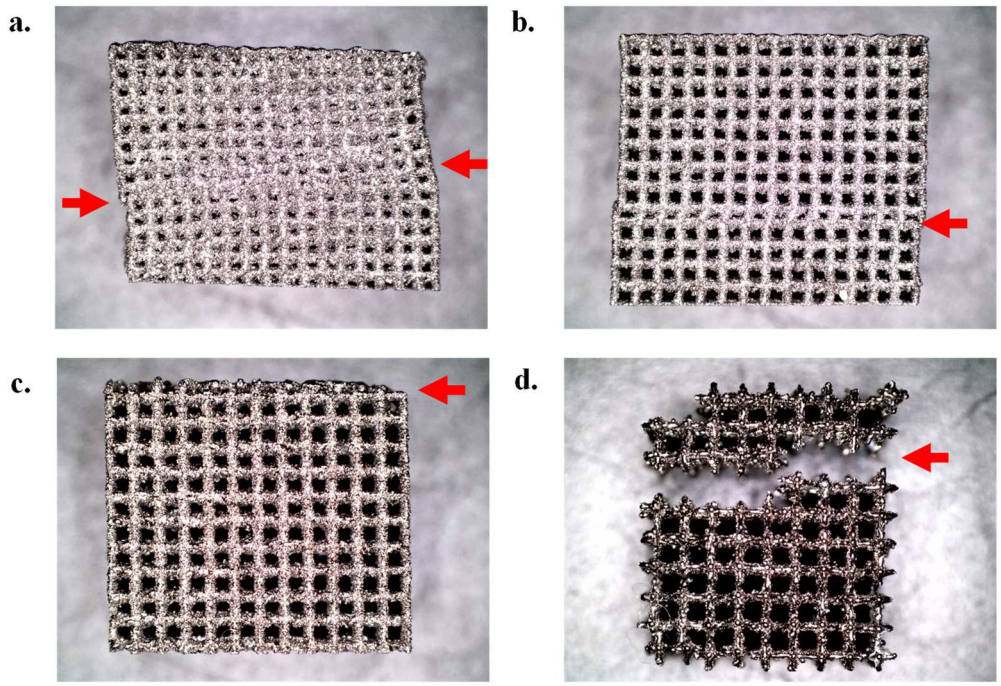

Figure 7. Compressive failure modes for cubic Ti-6Al-4V lattices. Pore sizes: (**a**) 400 µm, (**b**) 500 µm, (**c**) 600 µm, and (**d**) 900 µm. Reprinted from ref. [41]. Arrows indicate compressive failure.

In contrast, the BCC lattices under compressive loading exhibited diagonal shear failure along the 45° direction of the struts (Figures 8 and 9). Similar failures have been described for laser powder bed fusion manufactured lattices in the literature. He et al. [35] observed a 45° diagonal shear failure in selective laser-melted produced Ti-6Al-4V BCC lattices with a BCC unit cell having a modified variation with vertical struts. Maskery et al. [36] observed diagonal shear band failures in Ai-Si 10-Mg BCC lattices manufactured by selective laser melting.

For BCC 400 µm, it could not be visually verified that a 45° diagonal shear failure had occurred. Initial testing revealed that a 30 kN load cell was not sufficient. Additional testing with a 300 kN load cell was performed and it was found that multiple rows had collapsed, as seen in Figure 8a.

This failure mode for BCC 400 µm may be attributed to the extremely small pore size (~219 µm); however, this could not be determined from the corresponding stress–strain curve, as shown in Figure 10a.

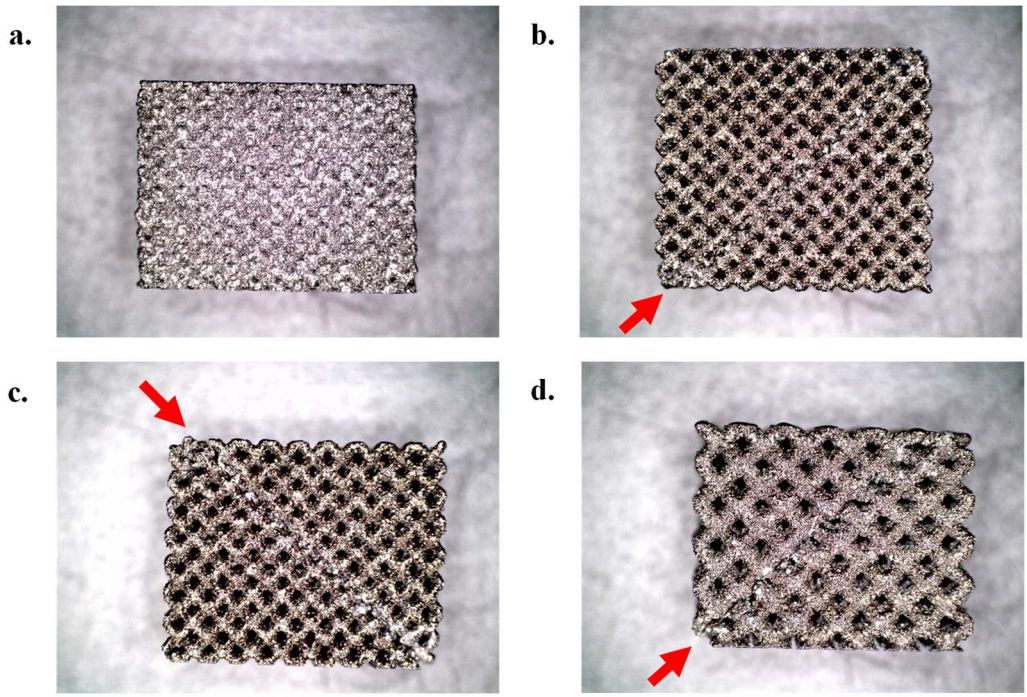

Figure 8. Compressive failure modes for body-centered cubic Ti-6Al-4V lattices. Pore sizes: (**a**) 400 µm, (**b**) 500 µm, (**c**) 600 µm, and (**d**) 900 µm. Reprinted from ref. [41]. Arrows indicate compressive failure.

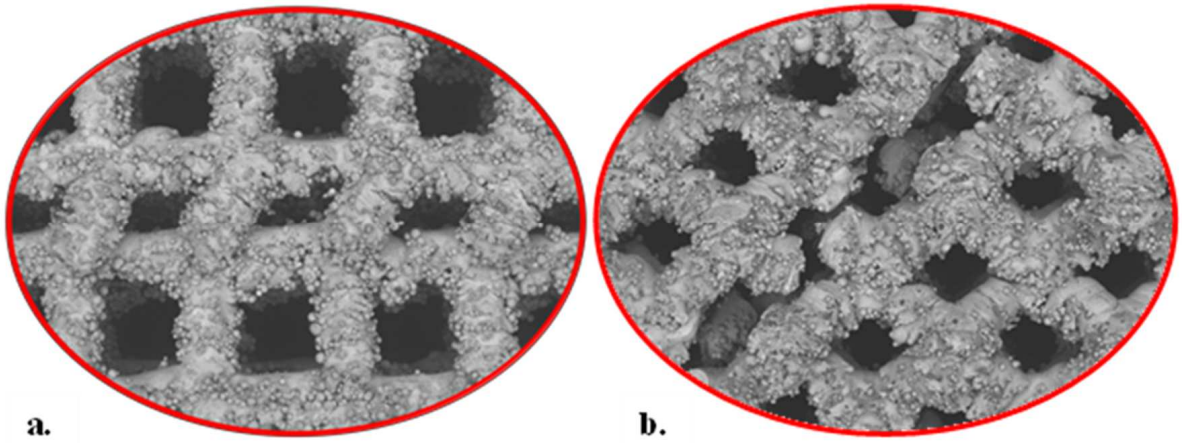

Figure 9. Enlarged SEM images detailing compressive failure mode for (**a**) Cubic 500 µm and (**b**) BCC 500 µm Ti-6Al-4V lattices. Reprinted from ref. [41].

The compressive stress–strain response for BCC and cubic lattices can be seen in Figures 10 and 11, respectively. Table 3 summarizes the compressive elastic modulus (E), yield strength (σ_y), and ultimate compressive strength (σ_{max}) for cubic and BCC lattices. Cubic lattices exhibited an E range of 185.2 to 843.3 MPa, whereas BCC lattices exhibited an E range of 710.8 to 996.1 MPa. All cubic and BCC lattices (with the exception of BCC 400 µm) fall within the E range of human cancellous bone of 10 to 900 MPa [52]. The highest E was observed for BCC 400 µm (996.1 $\pm$ 32.9 MPa) and the lowest E was found for Cubic 900 µm (185.2 $\pm$ 108.3 MPa). The large standard deviation for E Cubic 900 µm is due to significant variance across the three samples (75.9, 146.9, and 332.8 MPa).

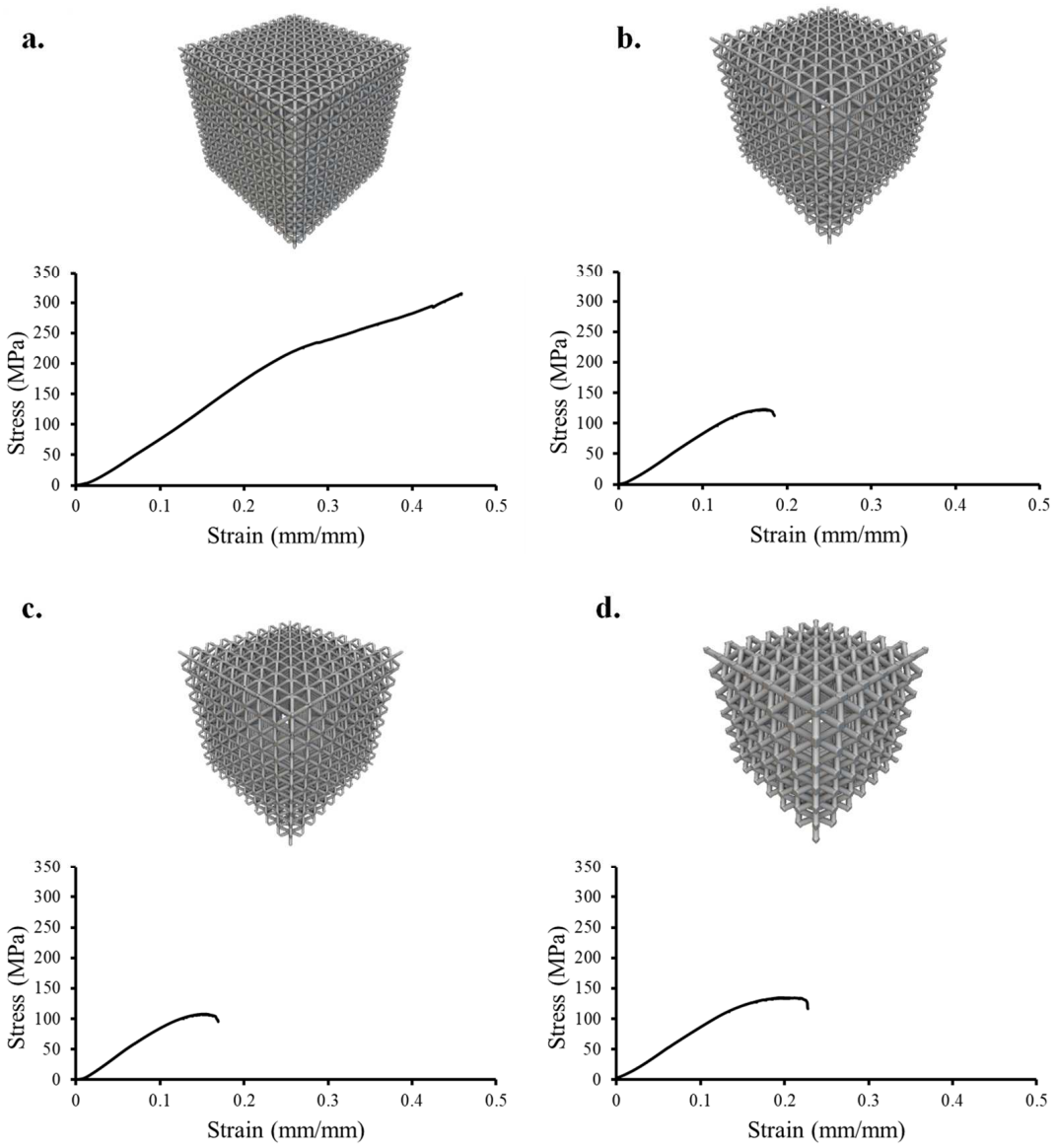

Figure 10. Compressive stress–strain curve for body-centered cubic lattices. Pore sizes: (**a**) 400 µm, (**b**) 500 µm, (**c**) 600 µm, and (**d**) 900 µm. Reprinted from ref. [41].

Table 3. Compressive mechanical properties for cubic and BCC lattices. Averaged value across three samples. Reprinted from ref. [41].

Lattice Type	Elastic Moduli—E (MPa)	Yield Strength—σ_y (MPa)	Compressive Strength—σ_{max} (MPa)
Cubic P400	843.3 (±32.9)	63.9 ± 11.2	221.2 ± 11.3
Cubic P500	685.5 (±77.9)	52.0 ± 21.2	111.6 ± 9.1
Cubic P600	632.1 (±80.0)	38.5 ± 7.1	78.5 ± 3.4
Cubic P900	185.2 (±108.3)	1.6 ± 0.5	6.9 ± 0.3
BCC P400	996.1 (±244.8)	73.4 ± 13.1	-
BCC P500	712.8 (±105.0)	58.4 ± 4.9	118.9 ± 2.7
BCC P600	710.8 (±155.1)	46.6 ± 1.2	103.9 ± 3.3
BCC P900	753.2 (±86.9)	34.1 ± 14.6	135.7 ± 1.4

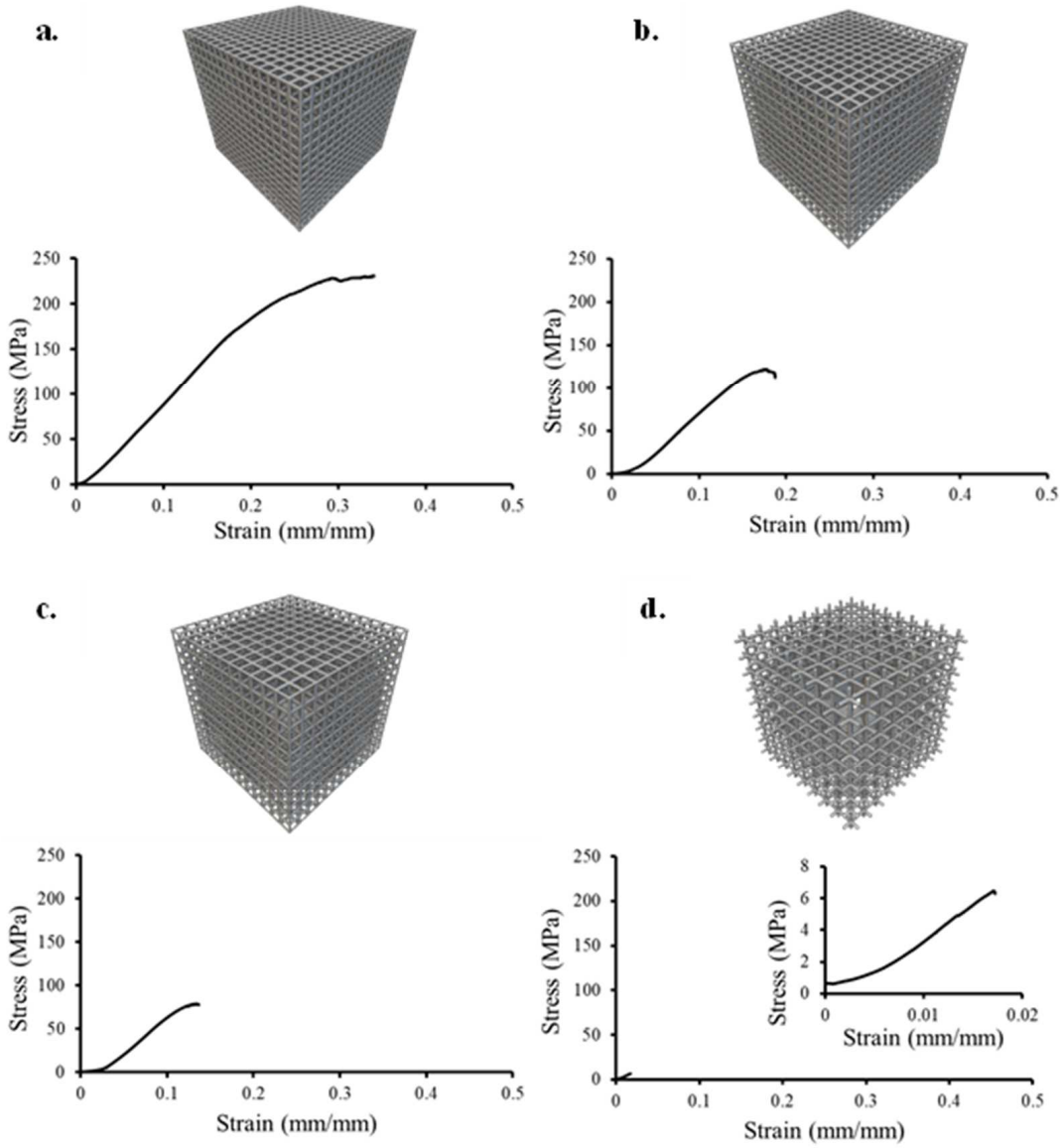

Figure 11. Compressive stress–strain curve for cubic lattices. Pore sizes: (**a**) 400 µm, (**b**) 500 µm, (**c**) 600 µm, and (**d**) 900 µm. Reprinted from ref. [41].

The σ_y range for all cubic and BCC lattices was 1.6 to 73.4 MPa, whereas the σ_y of cancellous bone is 0.6 to 16.3 MPa [53]. Cubic 900 µm is the only lattice that satisfies the σ_y criterion for cancellous bone. The σ_{max} range for all cubic and BCC lattices was 6.9 to 221.23 MPa whereas the σ_{max} of cancellous bone is 0.1 to 16 MPa [53–55]. Cubic 900 µm is the only lattice that satisfies this criterion. While most of the lattices do not meet human cancellous bone yield strength or compressive strength, the most important criterion that was met for all the lattice structures was the E range of human cancellous bone, as this has a direct effect on stress shielding [14]. It should be noted that the E of selective laser melted non-porous (solid) Ti-6Al-4V is 1163 MPa [56].

An additional metric to analyze the compressive properties of lattice structures is to evaluate the compressive strength at various relative densities, as shown in Figure 12 [47]. When comparing the relative density of cubic versus BCC specimens, the higher relative density found in BCC lattices results in an increase in σ_{max} when compared to cubic lattices. BCC lattices have superior compressive properties of E, σ_y, and σ_{max}, when compared to cubic lattices of similar pore size, which may be the result of the increased relative density observed in Figure 12.

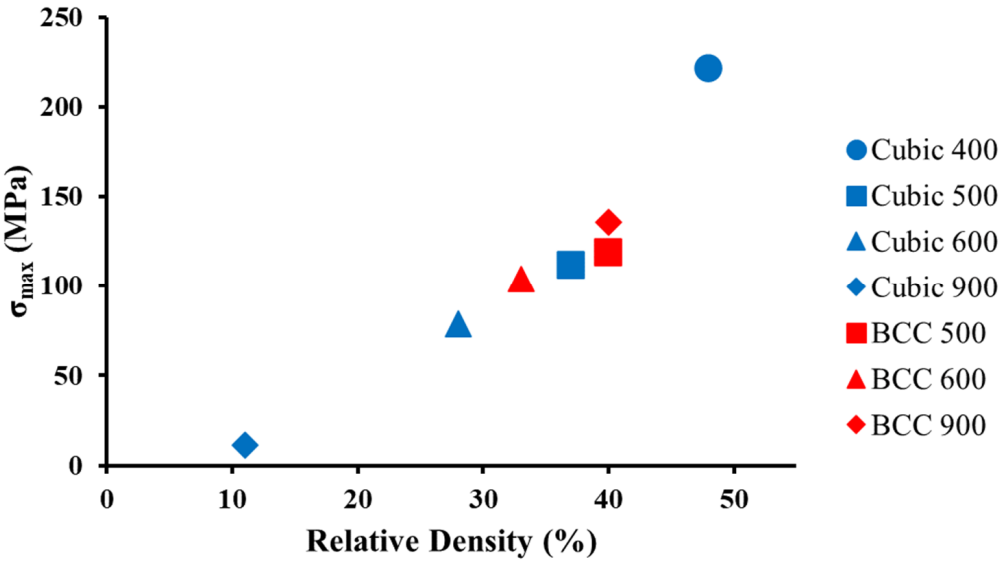

Figure 12. Compressive strength (σ_{max}) at printed relative densities corresponding to cubic and BCC lattices of varying porosity. Averaged value across three samples. Note: BCC 400 was omitted due to the lack of a σ_{max} value. Reprinted from ref. [41].

3.4. Tensile Response

An experimental pin-loaded feature was utilized in the design of selective laser-melted tensile specimens (Figure 3). Ti-6Al-4V tensile specimens were tested in the same vertical orientation (along the Z-axis) in which they were printed on the build plate. Manufacturing difficulties were experienced in producing three specimens per individual lattice without failures (Table 4). As a result, it was not possible to produce tensile specimens for cubic and BCC 400 µm.

Table 4. Tensile mechanical properties for cubic and BCC lattices with standard deviations. Values reflect the average across the number of samples specified. Reprinted from ref. [41].

Lattice Type	Number of Samples	Elastic Moduli—E (MPa)	Yield Strength—σ_y (MPa)	Tensile Strength—σ_{max} (MPa)
Cubic P400	0	-	-	-
Cubic P500	2	108.3 (±8.1)	7.1 (±2.6)	35.5 (±2.3)
Cubic P600	3	129.6 (±3.1)	5.3 (±0.5)	29.2 (±2.6)
Cubic P900	3	110.9 (±8.6)	4.5 (±0.3)	14.0 (±1.1)
BCC P400	0	-	-	-
BCC P500	2	109.2 (±0.8)	4.7 (±0.5)	21.9 (±2.3)
BCC P600	2	111.7 (±14.3)	3.4 (±0.2)	18.1 (±7.2)
BCC P900	2	92.7 (±4.2)	4.2 (±0.8)	13.3 (±6.7)

The failure mode for cubic and BCC specimens under tensile loading can be found in Figures 13 and 14, respectively. Two primary failure modes were observed. The first failure mode was a clean separation at the intersection of the uppermost grip and the gage, as found in Figure 13a for Cubic 500 µm. The second failure mode was partial or full separation at the first to third row, as seen in Figure 14 for all three BCC specimens. This type of failure mode could also be attributed to poor selective laser melting printing parameters, notably the inadequate binding of struts to the grip surface. Porter et al. [43] implemented the same tensile specimen design for BCC and voronoi tessellation method lattices in Nylon 12 and reported failures occurring in the gage area. In another study, Alsalla et al. [57] tested 316L stainless steel gyroid lattices manufactured by selective laser melting. Their tensile specimen exhibited failures near the solid end plates, which they believed was from the sudden change in density and stiffness, resulting in a stress

concentration. Wang et al. [37] created tensile testing specimens with selective laser melting using Inconel 718. The unit cell geometries were BCC, honeycomb, and TPMS lattices of various relative densities. Wang's tensile design included a solid shell with lattices in the middle of the tensile specimen. It was found that this solid shell had a direct effect on lattice mechanical properties. Their results indicated a linear relationship between tensile strength and relative density, which is similar to the work completed in the current research study (Figure 12).

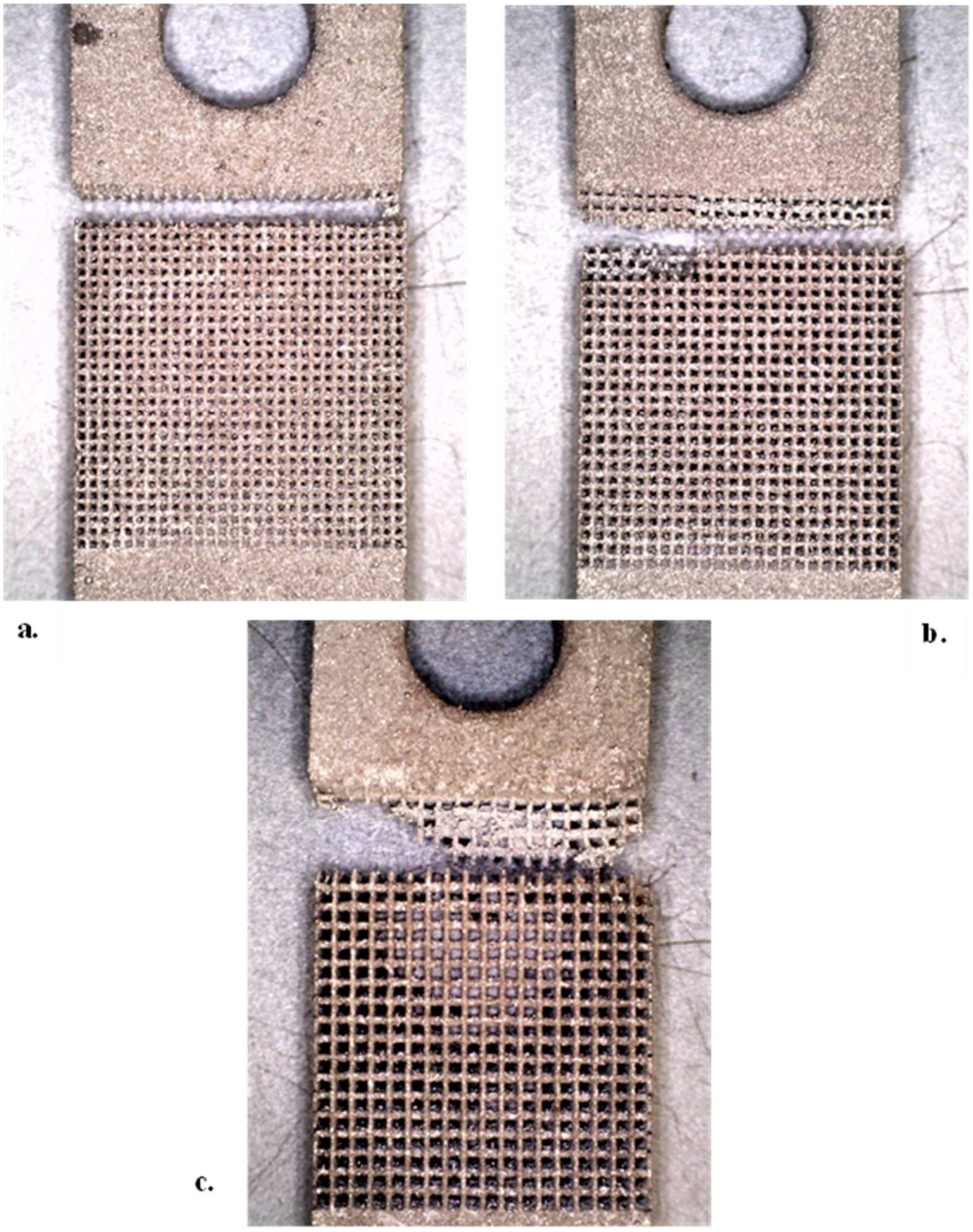

Figure 13. Tensile failure modes for cubic Ti-6Al-4V lattices. Pore sizes: (**a**) 500 μm, (**b**) 600 μm, and (**c**) 900 μm. Reprinted from ref. [41].

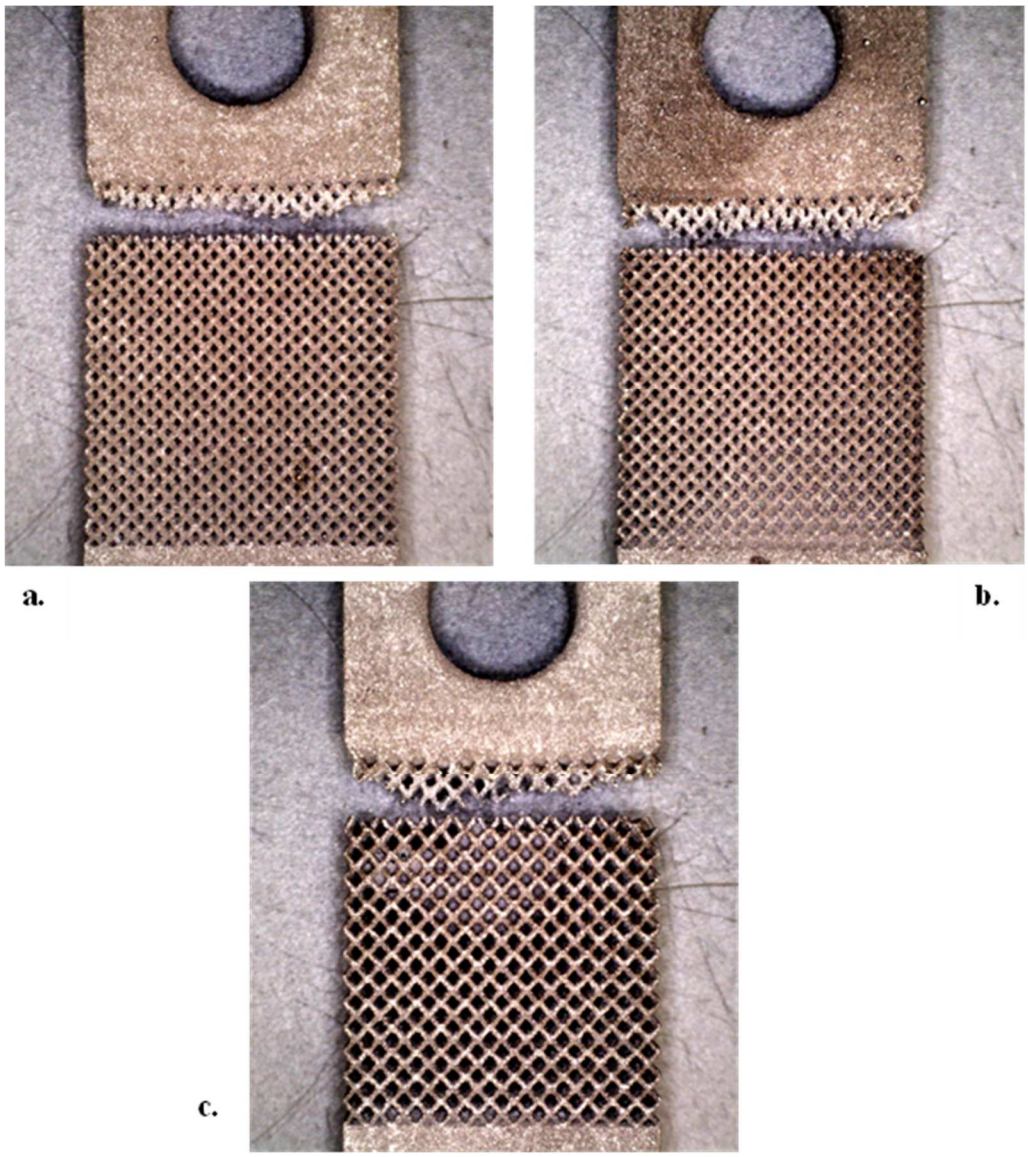

Figure 14. Tensile failure modes for body-centered cubic Ti-6Al-4V lattices. Pore sizes: (**a**) 500 µm, (**b**) 600 µm, and (**c**) 900 µm. Reprinted from ref. [41].

The tensile stress–strain response for cubic and BCC lattices can be seen in Figures 15 and 16, respectively. Table 4 summarizes the tensile modulus (E), yield strength (σ_y), and ultimate tensile strength (σ_{max}) for cubic and BCC lattices. The highest tensile E was observed for Cubic 600 µm (129.6 ± 8.6 MPa) and the lowest E for BCC 900 (92.7 ± 4.2 MPa). The E range is 92.7–129.6 MPa across all tensile specimens, which is within the E range of human cancellous bone (10 to 900 MPa) [52]. The tensile σ_y range for Cubic and BCC is 3.4–7.1 MPa, where all the lattices satisfy the σ_y range of cancellous bone (0.6 to 16.3 MPa) [53]. The tensile σ_{max} range is 13.3 to 35.5 MPa, which exceeds the tensile σ_{max} of human cancellous bone (0.92–5.38 MPa) [58]. In general, lattices with cubic strut geometries demonstrated higher values for tensile properties (E, σ_y, and σ_{max}) when compared to their BCC counterparts. It should be noted that for compression testing, the opposite was observed.

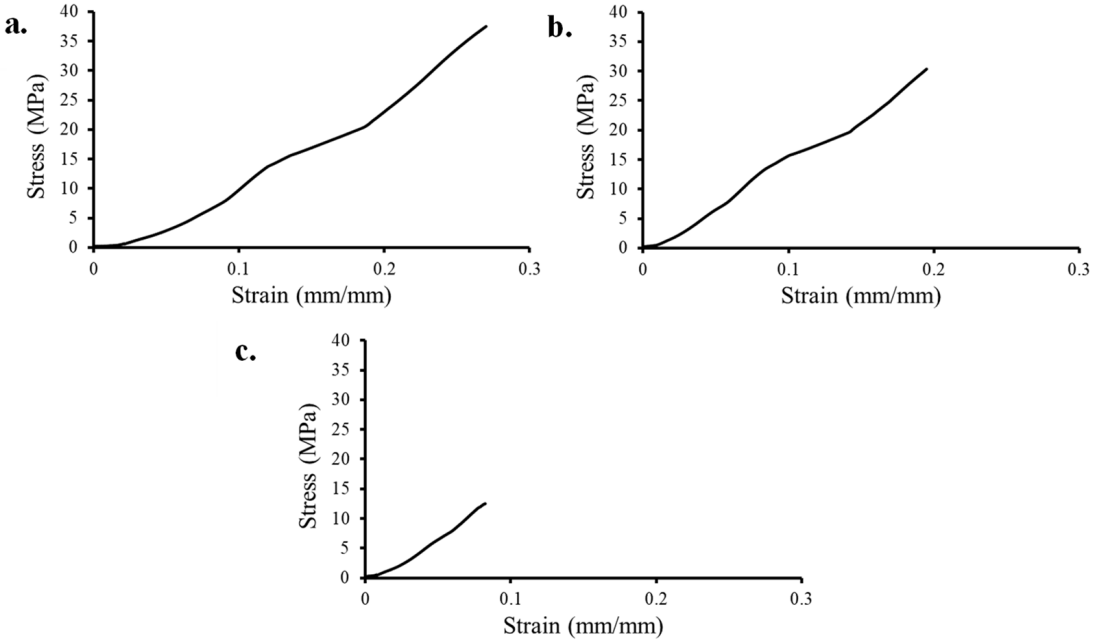

Figure 15. Tensile stress–strain curve for cubic Ti-6Al-4V lattices. Pore sizes: (**a**) 500 μm, (**b**) 600 μm, (**c**) 900 μm. Reprinted from ref. [41].

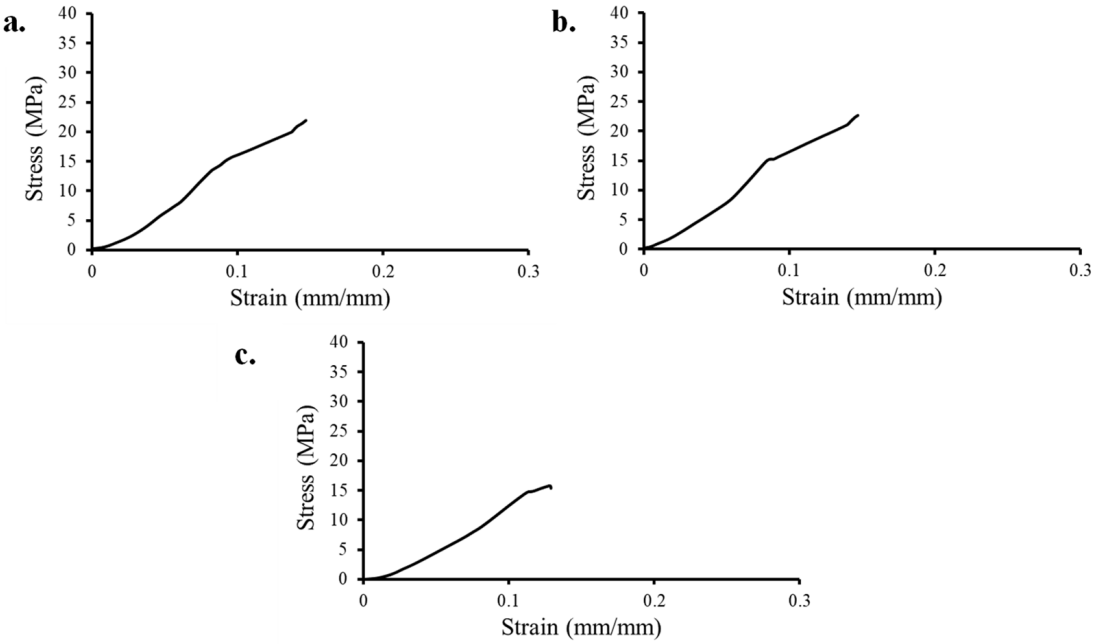

Figure 16. Tensile stress–strain curve for body-centered cubic Ti-6Al-4V lattices. Pore sizes: (**a**) 500 μm, (**b**) 600 μm, and (**c**) 900 μm. Reprinted from ref. [41].

3.5. Study Limitations

This study has demonstrated that cubic and BCC lattices of various pore sizes can satisfy the elastic modulus of human cancellous bone. However, it should be noted that the elastic modulus varies with different bones [52]. For example, the elastic modulus for femoral head cancellous bone is 900 ± 710 MPa, whereas the vertebral body elastic modulus is 165 ± 110 MPa [52]. It should be noted that the mechanical properties and microstructure of lattice structures will vary depending on process parameters of selective laser melting [59]. The lattice structure porosity, strut diameter, and unit cell geometry should be carefully designed to have an elastic modulus that is similar to the bone or joint

that it replaces. It is also important to note that orthopedic implants are integrated within the human body with fixture plates, screws, rods, and bone cements. As a result, the total ultimate strength and the elastic modulus will be greater than the individual components. In addition, as osteogenesis occurs internally in the lattice, this internal bone growth will affect load distribution.

Due to financial constraints, only a small number of compression and tensile specimens were produced, which resulted in a larger than desired standard deviation. In addition, since tensile specimen failures occurred near the fixture grips, future work should focus on alternative tensile designs for lattice structures. Lastly, as observed in the experimental setup for tensile testing (Figure 4), both ends of the tensile specimen grips are not perfectly aligned, which could contribute to a misaligned load on the tensile specimen.

4. Conclusions

In this work, the compressive and tensile properties of biomimetic lattice structures with a novel thin strut size (200 μm) were compared to that of cancellous bone for use in orthopedic applications. The key findings of this work are listed below.

1. Under compression, cubic lattices exhibit failure layer-by-layer, whereas BCC lattices display diagonal shear failure along the 45° direction of the struts. The elastic modulus range for cancellous bone (10 to 900 MPa) was matched by all pore sizes and unit cell geometries. Cubic 900 μm was the only lattice to satisfy the compressive yield strength (1.6 MPa) and compressive ultimate strength (6.9 MPa) of human cancellous bone (σ_y: 0.6 to 16.3 MPa and $\sigma_{\max}$: 0.1 to 16 MPa). BCC lattices displayed higher elastic modulus, compressive yield strength, and compressive ultimate strength than cubic lattices, due to higher relative density and superior unit cell geometry for compressive forces;
2. The experimental tensile specimen exhibited numerous failures near the grips, indicating that an alternative design should be explored in the future for metallic lattice structures. The tensile elastic modulus (92.7–129.6 MPa) and tensile yield strength (3.4–7.1 MPa) of all tensile lattice specimens were within the range of human cancellous bone (E: 10 to 900 MPa and σ_y: 0.6 to 16.3 MPa);
3. Structural characterization revealed that the relative density, weight, and strut diameter of selective laser melted parts were consistently larger than their corresponding CAD models for both cubic and BCC strut geometries due to selective laser melting resolution and unmelted powder adhesion.

Based on the results of this work, these lattice structures could be used as building blocks in 3D printing a patient-specific orthopedic implant, wherein the strut geometry and porosity of individual cells could be tuned in correlation to patient bone-density and loading parameters. Future work should include the optimization of AM build parameters and post-processing, as well as the incorporation of in situ process monitoring to observe for internal defects. In addition, the inclusion of finite element analysis simulation and Micro-CT analysis would provide invaluable data for how these lattices fail under loading.

Author Contributions: Conceptualization, D.P.P. and A.T.N.-D.; methodology, D.P.P., A.T.N.-D., D.S.E. and T.H.O.; validation, A.T.N.-D., M.F.P. and D.S.E.; formal analysis, D.P.P.; investigation, D.P.P.; resources, A.T.N.-D., M.F.P. and T.H.O.; data curation, D.P.P.; writing—original draft preparation, D.P.P.; writing—review and editing, A.T.N.-D., M.F.P. and D.S.E.; visualization, D.P.P.; supervision, A.T.N.-D.; funding acquisition, A.T.N.-D. All authors have read and agreed to the published version of the manuscript.

Funding: This work was supported by the Biomedical Engineering and Additive Mechatronics (BEAM) Lab directed by Amy Neidhard-Doll within the Department of Electrical and Computer Engineering at the University of Dayton.

Data Availability Statement: The data presented in this study are available on request from the corresponding author. The data are not publicly available due to privacy restrictions.

Acknowledgments: The authors would like to thank the University of Dayton Research Institute for assistance in manufacturing lattice structures and the use of Ti-6Al-4V powder. Special thanks to Gwendolyn Nuñez for editing assistance.

Conflicts of Interest: The authors declare no conflicts of interest.

References

1. Yan, C.; Hao, L.; Hussein, A.; Young, P.; Raymont, D. Advanced Lightweight 316L Stainless Steel Cellular Lattice Structures Fabricated via Selective Laser Melting. *Mater. Des.* **2014**, *55*, 533–541. [CrossRef]
2. Stoffelen, D.V.C.; Eraly, K.; Debeer, P. The Use of 3D Printing Technology in Reconstruction of a Severe Glenoid Defect: A Case Report with 2.5 Years of Follow-Up. *J. Shoulder Elb. Surg.* **2015**, *24*, e218–e222. [CrossRef] [PubMed]
3. Li, H.; Qu, X.; Mao, Y.; Dai, K.; Zhu, Z. Custom Acetabular Cages Offer Stable Fixation and Improved Hip Scores for Revision THA With Severe Bone Defects. *Clin. Orthop. Relat. Res.* **2016**, *474*, 731–740. [CrossRef] [PubMed]
4. Wong, K.C.; Kumta, S.M.; Geel, N.V.; Demol, J. One-Step Reconstruction with a 3D-Printed, Biomechanically Evaluated Custom Implant after Complex Pelvic Tumor Resection. *Comput. Aided Surg. Off. J. Int. Soc. Comput. Aided Surg.* **2015**, *20*, 14–23. [CrossRef] [PubMed]
5. Dhiman, S.; Sidhu, S.; Singh, P.; Bahraminasab, M. Mechanobiological Assessment of Ti-6Al-4V Fabricated via Selective Laser Melting Technique: A Review. *Rapid Prototyp. J.* **2019**, *25*, 1266–1284. [CrossRef]
6. Wang, X.; Xu, S.; Zhou, S.; Xu, W.; Leary, M.; Choong, P.; Qian, M.; Brandt, M.; Xie, Y.M. Topological Design and Additive Manufacturing of Porous Metals for Bone Scaffolds and Orthopaedic Implants: A Review. *Biomaterials* **2016**, *83*, 127–141. [CrossRef]
7. Dallago, M.; Raghavendra, S.; Luchin, V.; Zappini, G.; Pasini, D.; Benedetti, M. The Role of Node Fillet, Unit-Cell Size and Strut Orientation on the Fatigue Strength of Ti-6Al-4V Lattice Materials Additively Manufactured via Laser Powder Bed Fusion. *Int. J. Fatigue* **2021**, *142*, 105946. [CrossRef]
8. Soro, N.; Saintier, N.; Merzeau, J.; Veidt, M.; Dargusch, M.S. Quasi-Static and Fatigue Properties of Graded Ti–6Al–4V Lattices Produced by Laser Powder Bed Fusion (LPBF). *Addit. Manuf.* **2021**, *37*, 101653. [CrossRef]
9. Bai, L.; Gong, C.; Chen, X.; Zheng, J.; Yang, J.; Li, K.; Sun, Y. Heterogeneous Compressive Responses of Addi-tively Manufactured Ti-6Al-4V Lattice Structures by Varying Geometric Parameters of Cells. *Int. J. Mech. Sci.* **2022**, *214*, 106922. [CrossRef]
10. Tseng, S.-F.; Wang, I.-H.; Chang, C.-M.; Lee, C.-C.; Yeh, D.-Y.; Chen, T.-W.; Yeh, A.-C. Mechanical Character-istic Comparison of Additively Manufactured Ti–6Al–4V Lattice Structures in Biocompatible Bone Tissue Growth. *Mater. Sci. Eng. A* **2022**, *857*, 144045. [CrossRef]
11. Daynes, S.; Lifton, J.; Lu, W.F.; Wei, J.; Feih, S. Fracture Toughness Characteristics of Additively Manufactured Ti–6Al–4V Lattices. *Eur. J. Mech. A/Solids* **2021**, *86*, 104170. [CrossRef]
12. Jin, N.; Yan, Z.; Wang, Y.; Cheng, H.; Zhang, H. Effects of Heat Treatment on Microstructure and Mechanical Properties of Selective Laser Melted Ti-6Al-4V Lattice Materials. *Int. J. Mech. Sci.* **2021**, *190*, 106042. [CrossRef]
13. Cutolo, A.; Engelen, B.; Desmet, W.; Van Hooreweder, B. Mechanical Properties of Diamond Lattice Ti–6Al–4V Structures Produced by Laser Powder Bed Fusion: On the Effect of the Load Direction. *J. Mech. Behav. Biomed. Mater.* **2020**, *104*, 103656. [CrossRef] [PubMed]
14. Ridzwan, M.; Shuib, S.; Hassan, A.Y.; Ahmed Shokri, A.; Ibrahim, M. Problem of Stress Shielding and Improvement to the Hip Implant Designs: A Review. *J. Med. Sci.* **2007**, *7*, 460–467. [CrossRef]
15. Oftadeh, R.; Perez-Viloria, M.; Villa-Camacho, J.C.; Vaziri, A.; Nazarian, A. Biomechanics and Mechanobiology of Trabecular Bone: A Review. *J. Biomech. Eng.* **2015**, *137*, 108021–1080215. [CrossRef] [PubMed]
16. Kienapfel, H.; Sprey, C.; Wilke, A.; Griss, P. Implant Fixation by Bone Ingrowth. *J. Arthroplast.* **1999**, *14*, 355–368. [CrossRef] [PubMed]
17. Biemond, J.E.; Aquarius, R.; Verdonschot, N.; Buma, P. Frictional and Bone Ingrowth Properties of Engineered Surface Topographies Produced by Electron Beam Technology. *Arch. Orthop. Trauma Surg.* **2011**, *131*, 711–718. [CrossRef] [PubMed]
18. de Wild, M.; Schumacher, R.; Mayer, K.; Schkommodau, E.; Thoma, D.; Bredell, M.; Kruse Gujer, A.; Grätz, K.W.; Weber, F.E. Bone Regeneration by the Osteoconductivity of Porous Titanium Implants Manufactured by Selective Laser Melting: A Histological and Micro Computed Tomography Study in the Rabbit. *Tissue Eng. Part. A* **2013**, *19*, 2645–2654. [CrossRef] [PubMed]
19. Sing, S.L.; An, J.; Yeong, W.Y.; Wiria, F.E. Laser and Electron-Beam Powder-Bed Additive Manufacturing of Metallic Implants: A Review on Processes, Materials and Designs. *J. Orthop. Res.* **2016**, *34*, 369–385. [CrossRef]
20. Van Bael, S.; Chai, Y.C.; Truscello, S.; Moesen, M.; Kerckhofs, G.; Van Oosterwyck, H.; Kruth, J.-P.; Schrooten, J. The Effect of Pore Geometry on the In Vitro Biological Behavior of Human Periosteum-Derived Cells Seeded on Selective Laser-Melted Ti6Al4V Bone Scaffolds. *Acta Biomater.* **2012**, *8*, 2824–2834. [CrossRef]
21. Markhoff, J.; Wieding, J.; Weissmann, V.; Pasold, J.; Jonitz-Heincke, A.; Bader, R. Influence of Different Three-Dimensional Open Porous Titanium Scaffold Designs on Human Osteoblasts Behavior in Static and Dynamic Cell Investigations. *Materials* **2015**, *8*, 5490–5507. [CrossRef] [PubMed]
22. Valstar, E.R.; Nelissen, R.G.H.H.; Reiber, J.H.C.; Rozing, P.M. The Use of Roentgen Stereophotogrammetry to Study Micromotion of Orthopaedic Implants. *ISPRS J. Photogramm. Remote Sens.* **2002**, *56*, 376–389. [CrossRef]

23. Obaton, A.-F.; Fain, J.; Djemaï, M.; Meinel, D.; Léonard, F.; Mahé, E.; Lécuelle, B.; Fouchet, J.-J.; Bruno, G. In Vivo XCT Bone Characterization of Lattice Structured Implants Fabricated by Additive Manufacturing. *Heliyon* **2017**, *3*, e00374. [CrossRef] [PubMed]
24. Ran, Q.; Yang, W.; Hu, Y.; Shen, X.; Yu, Y.; Xiang, Y.; Cai, K. Osteogenesis of 3D Printed Porous Ti6Al4V Implants with Different Pore Sizes. *J. Mech. Behav. Biomed. Mater.* **2018**, *84*, 1–11. [CrossRef] [PubMed]
25. Taniguchi, N.; Fujibayashi, S.; Takemoto, M.; Sasaki, K.; Otsuki, B.; Nakamura, T.; Matsushita, T.; Kokubo, T.; Matsuda, S. Effect of Pore Size on Bone Ingrowth into Porous Titanium Implants Fabricated by Additive Manufacturing: An In Vivo Experiment. *Mater. Sci. Eng. C* **2016**, *59*, 690–701. [CrossRef] [PubMed]
26. Van der Stok, J.; Van der Jagt, O.P.; Amin Yavari, S.; De Haas, M.F.P.; Waarsing, J.H.; Jahr, H.; Van Lieshout, E.M.M.; Patka, P.; Verhaar, J.A.N.; Zadpoor, A.A.; et al. Selective Laser Melting-Produced Porous Titanium Scaffolds Regenerate Bone in Critical Size Cortical Bone Defects. *J. Orthop. Res.* **2013**, *31*, 792–799. [CrossRef] [PubMed]
27. Melchels, F.P.W.; Barradas, A.M.C.; van Blitterswijk, C.A.; de Boer, J.; Feijen, J.; Grijpma, D.W. Effects of the Architecture of Tissue Engineering Scaffolds on Cell Seeding and Culturing. *Acta Biomater.* **2010**, *6*, 4208–4217. [CrossRef] [PubMed]
28. Wally, Z.J.; Haque, A.M.; Feteira, A.; Claeyssens, F.; Goodall, R.; Reilly, G.C. Selective Laser Melting Processed Ti6Al4V Lattices with Graded Porosities for Dental Applications. *J. Mech. Behav. Biomed. Mater.* **2019**, *90*, 20–29. [CrossRef] [PubMed]
29. Wang, H.; Su, K.; Su, L.; Liang, P.; Ji, P.; Wang, C. The Effect of 3D-Printed Ti6Al4V Scaffolds with Various Macropore Structures on Osteointegration and Osteogenesis: A Biomechanical Evaluation. *J. Mech. Behav. Biomed. Mater.* **2018**, *88*, 488–496. [CrossRef] [PubMed]
30. Zhang, X.Z.; Leary, M.; Tang, H.P.; Song, T.; Qian, M. Selective Electron Beam Manufactured Ti-6Al-4V Lattice Structures for Orthopedic Implant Applications: Current Status and Outstanding Challenges. *Curr. Opin. Solid State Mater. Sci.* **2018**, *22*, 75–99. [CrossRef]
31. Yánez, A.; Cuadrado, A.; Martel, O.; Afonso, H.; Monopoli, D. Gyroid Porous Titanium Structures: A Versatile Solution to Be Used as Scaffolds in Bone Defect Reconstruction. *Mater. Des.* **2018**, *140*, 21–29. [CrossRef]
32. Parthasarathy, J.; Starly, B.; Raman, S.; Christensen, A. Mechanical Evaluation of Porous Titanium (Ti6Al4V) Structures with Electron Beam Melting (EBM). *J. Mech. Behav. Biomed. Mater.* **2010**, *3*, 249–259. [CrossRef] [PubMed]
33. Choy, S.Y.; Sun, C.-N.; Leong, K.F.; Wei, J. Compressive Properties of Ti-6Al-4V Lattice Structures Fabricated by Selective Laser Melting: Design, Orientation and Density. *Addit. Manuf.* **2017**, *16*, 213–224. [CrossRef]
34. Mullen, L.; Stamp, R.C.; Brooks, W.K.; Jones, E.; Sutcliffe, C.J. Selective Laser Melting: A Regular Unit Cell Approach for the Manufacture of Porous, Titanium, Bone in-Growth Constructs, Suitable for Orthopedic Applications. *J. Biomed. Mater. Res. B Appl. Biomater.* **2009**, *89*, 325–334. [CrossRef]
35. He, M.; Li, Y.; Yin, J.; Sun, Q.; Xiong, W.; Li, S.; Yang, L.; Hao, L. Compressive Performance and Fracture Mechanism of Bio-Inspired Heterogeneous Glass Sponge Lattice Structures Manufactured by Selective Laser Melting. *Mater. Des.* **2022**, *214*, 110396. [CrossRef]
36. Maskery, I.; Aboulkhair, N.T.; Aremu, A.O.; Tuck, C.J.; Ashcroft, I.A.; Wildman, R.D.; Hague, R.J.M. A Mechanical Property Evaluation of Graded Density Al-Si10-Mg Lattice Structures Manufactured by Selective Laser Melting. *Mater. Sci. Eng. A* **2016**, *670*, 264–274. [CrossRef]
37. Wang, X.; Wang, C.; Zhou, X.; Wang, D.; Zhang, M.; Gao, Y.; Wang, L.; Zhang, P. Evaluating Lattice Mechanical Properties for Lightweight Heat-Resistant Load-Bearing Structure Design. *Materials* **2020**, *13*, 4786. [CrossRef] [PubMed]
38. Bankoff, A.D.P. Biomechanical Characteristics of the Bone. In *Human Musculoskeletal Biomechanics*; Goswami, T., Ed.; InTech: London, UK, 2012; pp. 63–86.
39. Papazoglou, D.P. Additively Manufactured Lattice Structures for Orthopedic Implants—Analysis of Mechanical Properties. In Proceedings of the ASTM ICAM, Virtual, 16–20 November 2020.
40. Mazur, M.; Leary, M.; McMillan, M.; Sun, S.; Shidid, D.; Brandt, M. 5-Mechanical Properties of Ti6Al4V and AlSi12Mg Lattice Structures Manufactured by Selective Laser Melting (SLM). In *Woodhead Publishing Series in Electronic and Optical Materials*; Brandt, M.B.T.-L.A.M., Ed.; Woodhead Publishing: Sawston, UK, 2017; pp. 119–161, ISBN 978-0-08-100433-3.
41. Papazoglou, D.P. Additively Manufactured Ti-6Al-4V Biomimetic Lattice Structures for Patient-Specific Orthopedic Implants: The Effect of Unit Cell Geometry, Pore Size, and Pulsed Electromagnetic Field Stimulation on the Osseointegration of MG-63 Cells in Vitro, Mechanical Properties, and Surface Characterization. Ph.D. Thesis, University of Dayton, Dayton, OH, USA, 2023.
42. *ASTM Standard F3456-22*; Standard Guide for Powder Reuse Schema in Powder Bed Fusion Processes for Medical Applications for Additive Manufacturing Feedstock Materials. ASTM International: West Conshohocken, PA, USA, 2022.
43. Porter, D.A.; Di Prima, M.A.; Badhe, Y.; Parikh, A.R. Nylon Lattice Design Parameter Effects on Additively Manufactured Structural Performance. *J. Mech. Behav. Biomed. Mater.* **2022**, *125*, 104869. [CrossRef]
44. Ashby, M.F. The Properties of Foams and Lattices. *Philos. Trans. R. Soc. A Math. Phys. Eng. Sci.* **2005**, *364*, 15–30. [CrossRef]
45. *ASTM Standard E9-09*; Standard Test Methods of Compression Testing of Metallic Materials at Room Temperature. ASTM International: West Conshohocken, PA, USA, 2018.
46. *ASTM Standard E8/E8M-22*; Standard Test Methods for Tension Testing of Metallic Materials. ASTM International: West Conshohocken, PA, USA, 2022.
47. Maconachie, T.; Leary, M.; Lozanovski, B.; Zhang, X.; Qian, M.; Faruque, O.; Brandt, M. SLM Lattice Structures: Properties, Performance, Applications and Challenges. *Mater. Des.* **2019**, *183*, 108137. [CrossRef]

48. Yan, X.; Li, Q.; Yin, S.; Chen, Z.; Jenkins, R.; Chen, C.; Wang, J.; Ma, W.; Bolot, R.; Lupoi, R.; et al. Mechanical and in Vitro Study of an Isotropic Ti6Al4V Lattice Structure Fabricated Using Selective Laser Melting. *J. Alloys Compd.* **2019**, *782*, 209–223. [CrossRef]
49. Sombatmai, A.; Uthaisangsuk, V.; Wongwises, S.; Promoppatum, P. Multiscale Investigation of the Influence of Geometrical Imperfections, Porosity, and Size-Dependent Features on Mechanical Behavior of Additively Manufactured Ti-6Al-4V Lattice Struts. *Mater. Des.* **2021**, *209*, 109985. [CrossRef]
50. Vrána, R.; Koutecký, T.; Červinek, O.; Zikmund, T.; Pantělejev, L.; Kaiser, J.; Koutný, D. Deviations of the SLM Produced Lattice Structures and Their Influence on Mechanical Properties. *Materials* **2022**, *15*, 3144. [CrossRef] [PubMed]
51. Martinez, M.A.F.; Balderrama, Í.D.F.; Karam, P.S.B.H.; de Oliveira, R.C.; de Oliveira, F.A.; Grandini, C.R.; Vicente, F.B.; Stavropoulos, A.; Zangrando, M.S.R.; Sant'Ana, A.C.P. Surface Roughness of Titanium Disks Influences the Adhesion, Proliferation and Differentiation of Osteogenic Properties Derived from Human. *Int. J. Implant. Dent.* **2020**, *6*, 46. [CrossRef] [PubMed]
52. An, Y.; Draughn, R. *Mechanical Testing of Bone and the Bone–Implant Interface*; CRC Press: New York, NY, USA, 2000; ISBN 9780429125799.
53. Dunham, C.E.; Takaki, S.E.; Johnson, J.A.; Dunning, C.E. Mechanical Properties of Cancellous Bone of the Distal Humerus. *Clin. Biomech.* **2005**, *20*, 834–838. [CrossRef] [PubMed]
54. Hernandez, C.J.; Beaupré, G.S.; Keller, T.S.; Carter, D.R. The Influence of Bone Volume Fraction and Ash Fraction on Bone Strength and Modulus. *Bone* **2001**, *29*, 74–78. [CrossRef] [PubMed]
55. Keaveny, T.M.; Morgan, E.F.; Niebur, G.L.; Yeh, O.C. Biomechanics of Trabecular Bone. *Annu. Rev. Biomed. Eng.* **2001**, *3*, 307–333. [CrossRef] [PubMed]
56. Zhang, D.; Wang, L.; Zhang, H.; Maldar, A.; Zhu, G.; Chen, W.; Park, J.-S.; Wang, J.; Zeng, X. Effect of Heat Treatment on the Tensile Behavior of Selective Laser Melted Ti-6Al-4V by in Situ X-Ray Characterization. *Acta Mater.* **2020**, *189*, 93–104. [CrossRef]
57. Alsalla, H.; Hao, L.; Smith, C. Fracture Toughness and Tensile Strength of 316L Stainless Steel Cellular Lattice Structures Manufactured Using the Selective Laser Melting Technique. *Mater. Sci. Eng. A* **2016**, *669*, 1–6. [CrossRef]
58. Røhl, L.; Larsen, E.; Linde, F.; Odgaard, A.; Jørgensen, J. Tensile and Compressive Properties of Cancellous Bone. *J. Biomech.* **1991**, *24*, 1143–1149. [CrossRef]
59. Kaya, G.; Yıldız, F.; Korkmaz, İ.H.; Kaymaz, İ.; Yetim, A.F.; Ergüder, T.O.; Şen, Ç. Effects of Process Parame-ters on Selective Laser Melting of Ti6Al4V-ELI Alloy and Parameter Optimization via Response Surface Method. *Mater. Sci. Eng. A* **2023**, *885*, 145581. [CrossRef]